

Magnetic Flux Compression and The Experimental Design

Yuanjie Huang

Mianyang, 621900, China

Corresponding author's E-mail: hyj201207@163.com

Abstract: In this work, we investigate magnetic flux compression (MFC) process theoretically by means of Maxwell equations. On contrary to previous theoretical studies, the MFC process is found to be not described by magnetic diffusion equations. Also interestingly, it is revealed that a key dimensionless parameter named as magnetic Reynolds number (MRN) may determine the whole MFC process and dominate eddy electric field distribution within liner, temperature rise of liner, the increase of magnetic field enclosed by a liner and so on. At end of MFC, a larger MRN will bring a more obvious temperature rise and may cause a more rapid ablation for liner, which reversely inhibits increase of enclosed magnetic field. To reach the largest magnetic field, the MRN takes neither ultra-large nor quite small values, and a good strategy is that it may be designed to be ~ 100 . On the other hand, a notable Hall electrical voltage exists at the liner, chamber and sample, and it can reach thousands of voltage at end of MFC, and thereby pointing out the normal resistance detection method may not be suitable for measuring the sample resistance. Considering serious ablation of chamber and noticeable penetration of field into sample, a new detection method for probing insulator-metal transition of sample under isentropic compression was proposed, i.e., measuring temperature rise of sample in terms of instantaneous multi-channel spectrum radiation method. These theoretical analysis on MFC may

assist people to understand the physical processes and improve related experimental designs.

keywords: magnetic flux compression, magnetic Reynolds number, eddy electric field, Hall voltage, experimental design

1. Introduction

Magnetic flux compression (MFC) generators are devices which employ strong driving forces originating from high-energy explosives or large electrical current to push an electrically conductive liner to compress the trapped initial magnetic flux in the liner. They transform chemical energy of explosives or electrical energy into electromagnetic energy, and provide people an available route for generating a pulsed magnetic field up to 1000 T or higher. Since their start, they have attracted much attention in the world and have been widely used in multi-areas such as ultrahigh magnetic field research, high pressure science, oil and minerals exploration, mine detection, national defense and so on [1, 2, 3, 4, 5]. Through many-year development, some representative MFC generators were conceived and successfully constructed, for instance, disk generator, coaxial generator, parallel generator, helical generator and so on [1]. Of especially pointed out was the successful experimental design of very reproducible systems which were named as MC-1 generators [6, 7]. For action of these generators, the time-dependent magnetic field within a liner is vital during MFC processes. Because it not only leads to a notable temperature effect in the liner, but also affects the magnetic pressure exerting on the liner and therefore influences its dynamical state. Much experimental and theoretical efforts has been devoted to a precise description of the magnetic field evolution processes, for example, experimental methods using pickup coil and Faraday rotation for the typical experimental MFC generator with cylindrically conductive liners [8, 9]; a benchmarking computer code employing an electrical circuit model coupled with a

quasi-two-dimensional inductance and resistance calculation [10, 11] and other computer codes based on circuit analysis [12, 13]. However, the physical processes, especially time-dependent magnetic field strongly relying on the substantial magnetic flux losses induced by magnetic field diffusion is still unclear and sometimes was calculated by an empirical dimensionless flux loss parameter [10, 11].

In this work, we perform an analytical analysis of the electromagnetic processes in the operation of MFC with cylindrical liner (e.g. MC-1 apparatus) and thereby try to point out the basic principles of experimental design.

2. Theoretical Methods and Results

2.1 Analysis on liner

Let us consider an initial magnetic flux enclosed in a metallic cylindrical liner. For action of the liner, it will cut the magnetic lines, therefore resulting in notable eddy electric field (EEF) in the liner. The EEF in liner will induce a substantial eddy electrical current which offers a magnetic flux and impedes losses of magnetic flux within the liner, so that the magnetic flux will be conserved for an ideally conductive liner. It is the EEF that make the conservation of magnetic flux and to clarify time dependent of magnetic field, one must give the time-varying EEF distribution in the liner. In a word, EEF is the key.

In order to get EEF and the magnetic field in liner which is compressing the trapped magnetic flux, Maxwell Equations could be utilized. Take an assumption that the liner length is much larger than its radius, and this is usually satisfied in experimental designs.

$$\int \nabla \times \vec{E}(x',t) \cdot d\vec{s} = -\frac{\partial \phi(x,t)}{\partial t} \quad (1)$$

$$B(x,t) = \int_x^d \mu_0 \sigma(x',t) E(x',t) dx' + B_0 \quad (2)$$

where $\vec{E}(x,t)$ is time and position dependent of EEF in the liner, $B(x,t)$ is time and position dependent of magnetic field in the liner, μ_0 is vacuum permittivity, $\sigma(x,t)$ is time and position dependent of electrical conductivity of liner, d is liner thickness, B_0 is initial magnetic field, and the related flux equals

$$\phi(x,t) = B(0,t) \pi r^2 + \int_r^{r+x} B(r',t) 2\pi r' dr'. \text{ The schematic diagram is shown in Figure}$$

1. Of noted is that here position x and time t are two independent variables, although the liner thickness strongly depend on time. Based on Equation (1) and (2), one may easily obtain the two dominant equations

$$E(x,t) 2\pi(r+x) = B(x,t) 2\pi(r+x)v(t) - \pi r^2 \frac{\partial B(0,t)}{\partial t} - \int_0^x \frac{\partial B(x',t)}{\partial t} 2\pi(r+x') dx' \quad (3)$$

$$E(x,t) = -\frac{1}{\mu_0 \sigma(x,t)} \frac{\partial B(x,t)}{\partial x} \quad (4)$$

where $v(t)$ stands for magnitude of liner-inside flying velocity. Substitute Equation (4) into (3), it is

$$-\frac{(r+x)}{\mu_0 \sigma(x,t)} \frac{\partial B(x,t)}{\partial x} = B(x,t)(r+x)v(t) - \frac{r^2}{2} \frac{\partial B(0,t)}{\partial t} - \int_r^{r+x} \frac{\partial B(x',t)}{\partial t} (r+x') dx' \quad (5)$$

Performing the derivative on x , it is

$$\frac{1}{\mu_0 \sigma(x,t)} \left[\frac{\partial^2 B(x,t)}{\partial x^2} + \frac{1}{(r+x)} \frac{\partial B(x,t)}{\partial x} - \frac{\partial B(x,t)}{\partial x} \frac{\partial \ln \sigma(x,t)}{\partial x} \right] = \frac{\partial B(x,t)}{\partial t} - \left[\frac{B(x,t)}{r+x} + \frac{\partial B(x,t)}{\partial x} \right] v(t) \quad (6)$$

One may easily find that if the velocity of liner inside is zero and the electrical conductivity of liner is position independent, Equation (6) can degenerate to the

famous magnetic diffusion equation in cylindrical coordinates. Of emphasized is that the magnetic diffusion equation is not suitable for describing the MFC processes, because it neglects the position dependent of electrical conductivity due to temperature rise and motional liner cutting magnetic lines, i.e., the second term on right in Equation (6).

2.1.1 Eddy electric field

To capture the main physics and for simplicity, one may assume that the liner inside flies with a constant velocity v and an invariant electrical conductivity σ during MFC process. Thus, Equation (5) may be simplified to be

$$\frac{\partial B(u, \tau)}{2\eta \partial u} - \frac{(1-\tau)^2}{2(1-\tau+u)} \frac{\partial B(0, \tau)}{\partial \tau} - \frac{1}{1-\tau+u} \int_0^u \frac{\partial B(u', \tau)}{\partial \tau} (1-\tau+u') du' + B(u, \tau) = 0$$

where the liner inner radius is $r = r_0 - vt = r_0(1-\tau)$, $\tau = t/t_0$, $u = x/r_0$, dimensionless parameter $\eta = \mu_0 \sigma v r_0 / 2$, r_0 is initial inner radius of liner and t_0 could be regarded as total duration time of the MFC process. An acceptably approximated solution may be

$$E(u, \tau) \approx \frac{B_0 v}{\sqrt{\eta}} (1-\tau)^{-2+2/\sqrt{\eta}} e^{-2\sqrt{\eta}u} \quad (7)$$

According to Equation (7), position dependence of EEF at two specific time is shown in Figure 2 (a) and (b). As shown, the EEF continually increases with time and decreases with distance away from the liner inside. A larger parameter η for liner would cause a smaller EEF, which may be attributed to the fact that the magnetic flux confined by the liner with a larger parameter η decreases more slowly with time than that for a liner with a smaller parameter η .

Here $\eta = \mu_0 \sigma v r_0 / 2$ is a key parameter and analogous to the magnetic Reynolds

number [14, 15], so it is also named as magnetic Reynolds number (MRN).

2.1.2 Temperature rise

During the MFC processes, the EEF will inevitably result in a notable temperature rise for the liner. Based on Equation (7), the temperature rise can be easily obtained

$$\Delta T(u, \tau) = \frac{B_0^2}{\mu_0 C_v} e^{-4\sqrt{\eta}u} \frac{(1-\tau)^{-3+4/\sqrt{\eta}} - 1}{3-4/\sqrt{\eta}} \quad (8)$$

where C_v is specific heat capacity of liner. It can be seen that for the temperature rise, MRN also play a key role. For a definite MFC configuration with established liner structure and initial magnetic field, the temperature rise only depends on MRN and to one's surprise, the electrical conductivity and flying velocity of liner play an identical role. This conclusion also holds for the magnetic field variations in liner, which will be discussed afterwards. Time dependent of temperature rise is displayed in Figure 3. As shown, the temperature continuously increases with time and a larger MRN will cause a larger temperature rise. Also of observed is that at initial time the difference of temperature rise for liners with various MRN is small whereas the difference is more and more notable at the end of MFC process.

Due to the substantial temperature rise of liner during MFC, when one tries to design a related experimental apparatus such as MC-1, he/she must take into account the temperature rise seriously. A good method is to select a liner with relatively small MRN, which will be discussed later.

2.1.3 Ablation velocity

Substantial temperature rise will inevitably cause the ablation of liner inside. For simplicity, take the assumption that the MRN and specific heat capacity do not vary.

Thus the initial ablation time is

$$(1 - \tau_a)^{-1} \approx \left[\frac{\Delta T_a \mu_0 C_V}{B_0^2} e^{4\sqrt{\eta} u_a} (3 - 4/\sqrt{\eta}) \right]^{1/(3-4/\sqrt{\eta})} \quad (9)$$

where ΔT_a is temperature rise for ablation vaporization (once vaporization happens, the electrical conductivity of liner may almost decrease to zero.) and it is about 3000 K for many metals, τ_a is the reduced starting time for liner ablation at reduced position u_a . The reduced ablation position dependent of reduced time is shown in Figure 4(a). As is seen, the ablation starting time for liners increases with distance from liner inside, and decreases with increasing MRN, indicating that the ablation is much more serious for liners with larger MRN. For liners with smaller MRN, the distinction of ablation starting time for different positions of liner is smaller. This may originate from the much slow attenuation of EEF at liners with smaller MRN.

Resorting to Equation (9), the related ablation velocity can be easily obtained

$$v_a \approx \frac{v}{(1 - \tau_a)} \frac{3 - 4/\sqrt{\eta}}{4\sqrt{\eta}} \quad (10)$$

where v_a is ablation velocity. This velocity varies with position and MRN. The results are shown in Figure 4(b). As is shown, the ablation velocity continually increases with distance from liner inside, which may result from the rapid increase of reduced ablation time. For liners with bigger MRN, the ablation velocity in regions close to liner inside is smaller, as may result from their smaller ablation starting time.

For calculations in this part, the temperature dependent of liner electrical conductivity and time dependent of liner flying velocity, in another word, variations of MRN is not taken into account. Actually, they change in the MFC processes. The

liner electrical conductivity decreases owing to noticeable temperature rise and the liner inside velocity should be modified to be $v-v_a$ due to ablation velocity, both of which may cause a considerable reduction of MRN. Concluded is that once the ablation emerges the MRN dramatically falls off, making the liner invalid at end of MFC. Therefore, to avoid the ablation for MC-1 apparatus, one may try to design the liner with a relatively small MRN.

2.1.4 Magnetic field

Based on Equation (4) and (7), the position and time dependent of magnetic field could be obtained

$$B(u, \tau) \approx B_0 (1 - \tau)^{-2+2/\sqrt{\eta}} \left(1 - e^{-2\sqrt{\eta}u_d}\right) + B_0 \quad (11)$$

where parameter $u_d=d/r_0$ and d is liner thickness. Seen from this solution, the time and position dependent of magnetic field may mainly rely on MRN as well where the electrical conductivity and liner flying velocity also play the same role.

To check Equation (11), let us examine three special cases, one is $\eta \rightarrow 0$, the second one is $u_d \rightarrow 0$ and the third one is $\eta \rightarrow \infty$. (i) The electrical conductivity or liner flying velocity approaches zero, i.e., $\eta \rightarrow 0$. In this case, the magnetic field does not vary with time and position in the liner, and it is the initial magnetic field $B(x, t) = B_0$, indicating that the magnetic flux swept by liner entirely leaks. This conclusion is in agreement with actual situations that an insulating liner or a static liner cannot display MFC and the magnetic field is the initial magnetic field. (ii) The liner is quite thin, i.e., $u_d \rightarrow 0$. The magnetic field enclosed by the liner also approximates B_0 , suggesting that for MFC the liner should not be too thin and its thickness need to reach an appropriate

value $u > 1/2\sqrt{\eta}$. (iii) The electrical conductivity or liner flying velocity approaches infinite, i.e., $\eta \rightarrow \infty$. The magnetic field enclosed by the liner is $B(0, \tau) \approx B_0(1 - \tau)^{-2}$, giving ideal MFC and conservation of magnetic flux. These special cases may be in accord with nature, which may reversely verify the correctness of Equation (11).

For the general case, i.e., the liner with finite electrical conductivity, finite flying velocity and a large thickness, the magnetic field enclosed in the liner cavity is

$$B(0, \tau) \approx B_0(1 - \tau)^{-2+2/\sqrt{\eta}} \quad (12)$$

This enlightens people that the time-varying magnetic field within the liner cavity sensitively depend on the MRN for which the electrical conductivity, liner-inside flying velocity and initial inner radius of liner play the identical roles. A larger electrical conductivity, flying velocity and initial inner radius will yield a larger magnetic field.

Based on Equation (12), the time dependent of magnetic field for liner with different MRN is shown in Figure 5(a). Figure 5(a) displays that the magnetic field always increases with time and the liner with a larger MRN will generate a larger magnetic field. The increase of magnetic field may be mainly assigned to the diminution of electrical inductance of liner. Also shown is that at the beginning of MFC the distinction in trapped magnetic field for liner with different MRN is not obvious but the difference is very noticeable at the end, suggesting that the magnetic flux loss mainly happens at the end. This may be an important principle for the multi-cascade MC-1 apparatus, which will be addressed in the later parts.

In the previous discussion, variations of MRN is not touched on. In the actual MFC

process, it may decrease as MFC goes on. For many liners, the ablation starting time could be regarded as the end of MFC because its ablation velocity may approach and even exceed flying velocity of liner as shown in Figure 4 (b), causing abrupt reduction of MRN. Thus, the confined highest magnetic field B_h could be got in terms of Equation (9) and (12)

$$B_h \approx B_0 \left[\frac{\Delta T_a \mu_0 C_V}{B_0^2} (3 - 4/\sqrt{\eta}) \right]^{(2-2/\sqrt{\eta})/(3-4/\sqrt{\eta})} \quad (13)$$

where B_h is the highest magnetic field trapped in the liner. Based on this equation, the highest field depends on both MRN and initial field, as is shown in Figure 5(b). In the calculation, the ablation temperature takes 3000 K and specific heat capacity takes $3 \times 10^6 J/(K \cdot m^3)$, which are typical values for some conventional metals. This figure shows that for a liner thick enough, if the MFC process is ideal, meaning that no buckling happens and so on, the enclosed highest magnetic field increases with decreasing MRN and initial magnetic field, which may stem from weakening of ablation. This point enlightens people that it may be easy to achieve a higher magnetic field for a thick liner with a relatively smaller MRN value. However, if the buckling emerge, the situation may be much more complex and need to be investigated further.

2.1.5 Hall voltage at the liner

Owing to observable EEF and magnetic field at the liner, the free electrons in the liner will experience a Lorentz force. The free electrons may approach their equilibrium state very quickly, thus creating a Hall electric field and a Hall voltage across the liner thickness. According to Equation (7) and (11), the Hall voltage is derived easily

$$V_H(u, \tau) \approx \frac{B(u, \tau)[B(u, \tau) - B_0]}{2n_e q u_0} \quad (14)$$

where $V_H(u, \tau)$ is the Hall voltage at the liner, n_e is free electron density, q is absolute electric charge an electron carries, i.e., $1.6 \times 10^{-19} C$, u_0 is vacuum permittivity.

The Hall voltage monotonically rises with time and distance from the liner outside. And it may reach several tens of volts once the confined magnetic field within the liner cavity reaches $\sim 10^3 T$.

2.1.5 Electric force

Due to notable magnetic field and eddy electrical current at the liner, the free electrons undergo a Lorentz force F_l which may drive the electrons away from their ions. Upon reaching equilibrium state, a force F_e stemming from ion-electron attractive Coulomb interaction will balance Lorentz force. Its counterforce F_E exerts on the ions and accelerates them, as is shown in Figure 6. The force can be easily obtained $F_E = QE_H$, where Q is ion charge, E_H is Hall electric field. At equilibrium state the magnitude and direction of total counter force on all ions are the same as that of total Lorentz force on all electrons, respectively. It is $\sum_i q \vec{v}_i \times \vec{B} = \sum_j Q_j E_H$, where v_i is the i -th electron velocity, Q_j is j -th ion charge, i, j run over all electrons and ions, respectively. So, many people usually believe it is the Lorentz force that accelerates or decelerate the liners. However, here pointed out is that it is not the Lorentz force but the total electric force F_E on ions that accelerates or decelerate the liners.

In some situations the total Lorentz force F_l may be different from the total electric force F_E . For example, electrons are at the non-equilibrium state where Lorentz force is not balanced by ion-electron force F_e , and the situation may usually occurs at initial

time. Another situation may emerge when electron emission induced by strong Hall electric field and high temperature happens, meaning that the total electron charges is smaller than total ion charges. These complex situations should be researched and clarified in the future.

2.2 Analysis on sample chamber

For the metallic sample chamber, the magnetic field it experiences increases with time and also leads to a notable EEF at the chamber. The EEF not only screens magnetic field, but can also cause a large temperature rise and obvious ablation. These may inversely affect the time dependent of magnetic field and thus bring alterations to EEF further. They are very complex processes. To treat these processes, it is reasonable to first take a magnetic field versus time relation such as Equation (12). This time dependent of magnetic field may distinct from the real field, but it can be employed to explore the key features of chamber and sample in MFC process.

2.2.1 Magnetic field at sample chamber

During MFC process for MC-1 apparatus, the EEF in metallic sample chamber could be described by

$$E_t(x,t) = \frac{1}{\mu_0 \sigma_t(x,t)} \frac{\partial B_t(x,t)}{\partial x} \quad (14)$$

$$E_t(x,t) 2\pi(r_t - x) = - \left[\begin{aligned} &\pi(r_t - d)^2 \frac{\partial B_t(d,t)}{\partial t} + \int_x^d \frac{\partial B_t(x',t)}{\partial t} 2\pi(r_t - x') dx' \\ &+ B_t(d,t) 2\pi(r_t - d) \frac{\partial r_t}{\partial t} + \int_x^d B_t(x',t) 2\pi \frac{\partial r_t}{\partial t} dx' \end{aligned} \right] \quad (15)$$

where $E_t(x,t)$ and $B_t(x,t)$ is position and time dependent of EEF and magnetic field at the metallic sample chamber, respectively, $\sigma_t(x,t)$ is position and time dependent of

electrical conductivity of chamber, r_t and d is outer radius and thickness of the chamber, respectively. In MFC processes, the moving velocity of sample chamber may be very small and is ignored here, so Equation (15) can be written as

$$\frac{2\pi(r_t - x)}{\mu_0\sigma_t(x,t)} \frac{\partial B_t(x,t)}{\partial x} = - \left[\pi(r_t - d)^2 \frac{\partial B_t(d,t)}{\partial t} + \int_x^d \frac{\partial B_t(x',t)}{\partial t} 2\pi(r_t - x') dx' \right] \quad (16)$$

Ignore the position dependence of electrical conductivity and perform the differential on x , one may get

$$\frac{1}{\mu_0\sigma_t} \left[\frac{\partial^2 B_t(x,t)}{\partial x^2} - \frac{1}{r_t - x} \frac{\partial B_t(x,t)}{\partial x} \right] = \frac{\partial B_t(x,t)}{\partial t} \quad (17)$$

For simplicity, the time dependent of magnetic field enclosed by liner takes the same form as Equation (12). Thus, an acceptable approximate solution may be

$$B_t(x,t) \approx B_0 \left(1 - \frac{t}{t_0}\right)^{-1+1/\sqrt{\eta}} \left(1 - \frac{t}{t_0} + \frac{\mu_0\sigma_t(2r_t - x)x}{4t_0}\right)^{-1+1/\sqrt{\eta}} \quad (18)$$

where t_0 is total duration time of MFC. This solution may be examined from several respects. (1) For the outer side of the metallic sample chamber, *i.e.*, $x=0$, the magnetic field is the same as that enclosed by the liner; (2) the electrical conductivity of chamber reaches infinite, $\sigma_t \rightarrow \infty$, the magnetic field could be entirely screened by a very thin layer of chamber; (3) the electrical conductivity of chamber is very small, $\sigma_t \rightarrow 0$, the magnetic field the whole chamber undergoes is also the field enclosed by the liner. These cases may be consistent with actual physical situations, indicating rationality of the solution.

Take a 1 mm thick copper chamber with radius $r_t=5$ mm as an example and the magnetic field outside the chamber takes the form $B(t) = B_0(1-t/t_0)^{-2+2/5}$. Thus, the magnetic field at the chamber, varying with time and position, is shown in Figure 7.

It displays that the magnetic field increases with time but continuously drops with distance from the chamber outside due to screening. Here of noted is that the decrease of electrical conductivity of chamber owing to substantial temperature rise is not taken into account. In actual case, decrease of electrical conductivity may reduce the screening, resulting in a relatively uniform magnetic field distribution at the chamber and a much larger field at the sample.

2.2.2 EEF at sample chamber

Based on equation (18), the corresponding EEF at the metallic chamber can be obtained easily

$$E_t(x,t) = B_0 \left(1 - \frac{t}{t_0}\right)^{-1+1/\sqrt{\eta}} \left[1 - \frac{t}{t_0} + \frac{\mu_0 \sigma_t (2r_t - x)x}{4t_0}\right]^{-2+1/\sqrt{\eta}} \frac{r_t - x}{2t_0} (-1+1/\sqrt{\eta}) \quad (19)$$

This solution is also checked in several cases. First, in case of infinite electrical conductivity $\sigma_t \rightarrow \infty$, the EEF decreases sharply to zero within a very thin layer, i.e., totally screening. Second, for the chamber outside, i.e., $x=0$, as expected, EEF is proportional to radius and derivative of magnetic field on time. Third, in case of a chamber with infinite radius and thickness, $r_t \rightarrow \infty$ and $x \rightarrow \infty$, the EEF may be zero based on Equation (19) because of screening. These cases may be in accord with real physics, demonstrating that the equation (18) is a good solution.

In general cases, based on Equation (19), the EEF not only relies on chamber configuration, including its radius and thickness, but also depends on its electrical conductivity and the MFC duration time. The EEF decreases gradually along the chamber thickness, and a large electrical conductivity will cause a smaller EEF at the chamber. Also in agreement with variation of magnetic field at the chamber, a much

longer MFC duration would yield a relatively smaller EEF, which may be propitious to avoid serious temperature rise and the related ablation.

2.2.3 Temperature rise

Due to the notable EEF at the chamber, as anticipated, a substantial temperature rise would be induced. Based on Equation (19), it may be written as

$$\Delta T_t(x, t) = \frac{\sigma_t B_0^2 (r_t - x)^2}{2C_{tV} 4t_0} \left(-1 + 1/\sqrt{\eta}\right)^2 \int_0^\tau (1 - \tau')^2 \times \left\{ (1 - \tau')^2 + \frac{[2r_t - x_a(\tau')] x_a(\tau')}{r_0^2} + \frac{\mu_0 \sigma_t (1 - \tau') [2r_t - x - x_a(\tau')] [x - x_a(\tau')]}{4t_0} \right\}^{-4+2/\sqrt{\eta}} d\tau'$$

where ΔT_t is temperature rise at the chamber, C_{tV} is specific heat capacity of chamber, $x_a(t)$ is time dependent of ablation thickness at the chamber. For many experimental designs, a cooper chamber is usually selected [1, 16]. A typical relation between time and ablation thickness is shown in Figure 8 (a). In the calculations, the time dependent of magnetic field takes the form $B(0, \tau) \approx B_0 (1 - \tau)^{-1.6}$, and the initial magnetic field B_0 takes 5 T. The outer radius of chamber takes 5 mm. Of emphasized is that in many experiments the actual time dependent of field and initial field may distinct from them, but the underlying physics and principle for the experimental design can still be revealed. For a chamber with larger electrical conductivity, the ablation happens earlier. As the magnetic field continuously increases, the ablation thickness of chamber with larger electrical conductivity may also be larger.

2.2.4 Ablation velocity

As is shown in Figure 8, the ablation thickness of a copper chamber varies with reduced time, and can be described approximately by $x_a(\tau) \approx \exp(20.6\tau - 17.8)$ and $x_a \approx \exp(26.3\tau - 24.4)$ for chamber with different electrical conductivity $6 \times 10^7 \text{ s/m}$ and $6 \times 10^6 \text{ s/m}$, respectively. Hence, the corresponding ablation velocity can be got easily, $v(x) = 20.6x_a/t_0$ and $v(x) = 26.3x_a/t_0$. In the calculation the electrical conductivity takes a constant value, despite that they actually decreases gradually with temperature rise. The real ablation thickness and ablation velocity may be a little different from the calculated values, but this calculation may still grasp the main physics.

Concluded is that as the ablation begins, the ablation velocity monotonically increases with the ablation thickness. Here a typical ablation velocity value is estimated. For ablation thickness $\sim 1 \text{ mm}$, the related ablation velocity could reach several km/s in the MFC process. Reversely, the ablation will reduce the magnetic field outside the chamber, resulting in an existence of a highest magnetic field in the MFC. The magnetic flux on the chamber is

$$\phi_t(\tau) = \frac{4\pi t_0 \sqrt{\eta}}{\mu_0 \sigma_t} \frac{B_0}{(1-\tau)} \left\{ \begin{array}{l} \left[(1-\tau)^2 + \frac{(2r_i - x_a)x_a}{r_0^2} + \frac{\mu_0 \sigma_t (1-\tau)(2r_i - d)d}{4t_0} \right]^{1/\sqrt{\eta}} \\ - \left[(1-\tau)^2 + \frac{(2r_i - x_a)x_a}{r_0^2} + \frac{\mu_0 \sigma_t (1-\tau)(2r_i - x_a)x_a}{4t_0} \right]^{1/\sqrt{\eta}} \end{array} \right\}$$

And the magnetic flux within the chamber is

$$\phi_c(\tau) = \pi(r_i - d)^2 B_0 \left[(1-\tau)^2 + \frac{(2r_i - x_a)x_a}{r_0^2} + \frac{\mu_0 \sigma_t (1-\tau)(2r_i - d - x_a)(d - x_a)}{4t_0} \right]^{-1+1/\sqrt{\eta}}$$

So related effective area for the magnetic flux is $S(\tau) = [\phi_t(\tau) + \phi_c(\tau)] / B_0 (1-\tau)^{-2+2/\sqrt{\eta}}$.

The modified magnetic field outside the chamber might be

$$B(\tau) \approx B_0 \left[(1-\tau)^2 + S(\tau) / \pi r_0^2 + (2r_t - x_a) x_a / r_0^2 \right]^{-1+1/\sqrt{\eta}} \quad (20)$$

According to this expression, the existence of sample chamber will reduce the related magnetic field conspicuously because of serious ablation and field penetration into sample at the end of MFC. As a result, the applied pressure on the chamber is strongly limited. A typical resultant magnetic field versus reduced time (The calculation ignores effective area $S(\tau)$.) is given by Figure 9. If the chamber radius and thickness take 5 mm and 1 mm, respectively, it is very difficult for the finally obtained highest magnetic field outside the chamber to exceed 400 T. Thus the magnetic pressure applied on the chamber outside may not reach 70 GPa.

Of noted is that the weakened magnetic field outside the chamber may decrease both the temperature rise and related ablation further, which reversely improve the magnetic field, finally approaching the actual physical process by many iterations. Here for sake of simplicity and grasping main physics in MFC, only first-order approximation is given in the discussion.

2.2.5 Hall voltage

Like the case of liner, a Hall voltage (HV) is also caused at the chamber and the sample. The HV at chamber is

$$V_{iH} = \frac{B^2(\tau, 0) - B^2(\tau, d)}{2\mu_0 n_e q} \quad (21)$$

where n_{ie} is free electron density in the chamber, q stands for electron charge, d is chamber thickness. The magnetic field entering the sample $B(\tau, d)$ is

$$B(\tau, d) \approx B_0 \left\{ (1-\tau)^2 + \frac{(2r_t - x_a)x_a}{r_0^2} + \frac{\mu_0 \sigma_t (1-\tau) [2r_t - d - x_a(\tau)] [d - x_a(\tau)]}{4t_0} \right\}^{-1+1/\sqrt{\eta}} \quad (22)$$

where x_a is ablation thickness of chamber. This field varies with time and ablation as shown in Figure 10(a). As is seen, the magnetic field penetrating into the sample gradually increases with reduced time and a remarkable upturn occurs when the chamber is totally ablated. The HV existing at the sample along its radius is

$$V_{sH} = \frac{\mu (r_t - d)^2}{8} \frac{\partial B^2(\tau, d)}{\partial t} \quad (23)$$

where μ denotes carrier mobility in the sample. For many non-conducting samples (semiconductor and insulators), carrier mobility is in a range 10^3 - 10^5 cm^2/Vs [17], so that the HV at the sample may range from 10^3 to 10^4 V at end of MFC, as is shown in Figure 10 (b). It displays that the HV monotonically increases with reduced time and exhibits a sudden increase upon entire ablation of chamber. The emergence of HV at the chamber and non-conducting sample will place a big obstacle for the resistance measurement. However, in the related experiments [1], HV has not been taken into account seriously. As a result, the resistance measurement may neglect this main problem and the obtained results in such experiments can not give the accurate resistance of sample under compression in the chamber.

2.3 Multi-cascade MFC

For multi-cascade MFC setup, the cascade consists of enamel-coated straight metal wires and is transparent to the axial magnetic field [18]. However, once a shock wave

passes over it, the cascade becomes electrically conductive along its ring, thus compressing the enclosed magnetic flux as a liner. Based on the discussion on temperature rise and the related ablation for liners, the temperature rise for a cascade may be

$$\Delta T(u, \tau) = \frac{B_0^2}{\mu_0 C_V} e^{-4\sqrt{\eta}u} \frac{(1-\tau_f)^{-3+4/\sqrt{\eta}} - (1-\tau_i)^{-3+4/\sqrt{\eta}}}{3-4/\sqrt{\eta}}$$

where τ_f and τ_i are two instantaneous reduced time at which the related cascade starts to compress magnetic flux and collides to next cascade, respectively. It is easy to find that the greatest temperature rise may happen at end of MFC. Therefore, to avoid conspicuous ablation the inner cascade must be very close to sample chamber. In all, the usage of multi-cascade can efficiently avoid ablation, thereby maintaining a high MRN and resulting in a much higher magnetic field. Of noted is that when one examines the actual temperature rise of cascades, besides temperature rise caused by eddy electric currents, he/she must take into account the temperature rise due to shock wave compression.

3. Experimental design

3.1 Experimental design of liner

As for liner, according to previous calculation and discussion, its design should refer to MRN. MRN should be neither too large nor too small, otherwise, the magnetic field enclosed by liner can't reach a high value because of either serious ablation or noticeable magnetic flux leakage. Liner material may be selected to ensure the MRN approaches about 100 initially. For a liner with inner radius 50 mm, flying velocity 5 km/s, the titanium alloy TC4 may be a good candidate. This alloy exhibits

several appropriate properties. First, its melting point and boiling point is very high; second, it displays large mechanic strength, enabling liner buckling weaken; third, its density is relatively small, which is easy to drive; fourth, compared with other metals, its electrical conductivity is quite low, effectively reducing temperature rise and subsequent ablation.

According to previous discussion on multi-cascade MFC apparatus, more cascades may avoid the dramatic temperature rise to some extent and therefore result in a much higher enclosed magnetic field. One may conceive that if there are so many cascades that no gap exists between two nearby cascades, meaning that the cascades form a very thick one whose inner surface and outer surface almost approaches sample chamber and magnetic solenoid, respectively, which is shown in Figure 11. Upon penetration of shock waves into this cascade, the metal wires subject to shock waves may weld rapidly and form an isotropically conductive cylinder. Then, it acts as a liner, trapping and compressing the enclosed magnetic flux. As shock wave propagates in the cascade further, the liner becomes much thicker and the newly formed inner parts of liner compress the magnetic flux subsequently, as shown in Figure 12. This supreme cascade may maintain a large MRN and efficiently avoid serious ablation at end of MFC process.

In actual cases, to reach the expected targets, the supreme cascade should be designed to suppress the related dynamical instability and jetting during the whole MFC process.

3.2 Experimental design of sample chamber

To get a high pressure within the sample chamber, its design is of paramount importance. The main hindrance may arise from the ablation and magnetic flux entering the chamber. The two factors are paradoxical. To avoid ablation, one may try to employ a metal with low electrical conductivity, however, it will inevitably lead to a strong penetration of magnetic flux into the chamber, i.e., causing a large effective area for magnetic flux $S(\tau)$. If one intends to utilize a metal with high electrical conductivity as the chamber, a much more serious ablation will arise in spite of its much smaller effective area $S(\tau)$. An acceptable scheme may use a metal with both large electrical conductivity and high vaporization point, meanwhile decreasing chamber radius and increasing its thickness slightly.

4. Detection

4.1 Resistance measurement on samples

Considering strong and complex electromagnetic environments in MFC process, especially existence of HV at chamber and sample, it is quite difficult to measure resistance of sample by means of classical methods.

In this work, a new method for measuring insulator-metal transition (IMT) was proposed in MFC process. Owing to finite thickness and electrical conductivity of chamber, magnetic flux inevitably enter the sample, creating a magnetic field. This field also varies rapidly, yielding a notable eddy electrical current in the sample. The induced temperature rise may be

$$\Delta T_s = \frac{\sigma_s r^2}{8C_{sV} t_0} \int_0^\tau \left[\frac{\partial B(\tau', d)}{\partial \tau'} \right]^2 d\tau' \quad (24)$$

where σ_s is electrical conductivity of sample, r is distance from sample center, C_{sV} is

specific heat capacity of sample, ΔT_s is related temperature rise for sample. Substitute equation (22) into equation (24), one may obtain

$$\Delta T_s = \frac{\sigma_s r^2 B_0^2}{8C_{sV} t_0} \left(1 - 1/\sqrt{\eta}\right)^2 \int_0^\tau \left\{ (1-\tau)^2 + \frac{(2r_i - x_a)x_a}{r_0^2} + \frac{\mu_0 \sigma_t (1-\tau) [2r_i - d - x_a(t)] [d - x_a(t)]}{4t_0} \right\}^{-4+2/\sqrt{\eta}} \\ \times \left\{ -2(1-\tau) + \frac{2(r_i - x_a)}{r_0^2} \frac{\partial x_a}{\partial \tau} - \frac{\mu_0 \sigma_t (2r_i - d - x_a)(d - x_a)}{4t_0} + \frac{\mu_0 \sigma_t (1-\tau) 2(r_i - x_a)}{4t_0} \frac{\partial x_a}{\partial \tau} \right\}^2 d\tau'$$

It can be easily found that if the sample is non-conducting, this temperature rise may be negligible. However, once IMT occurs and chamber is almost ablated, the temperature rise may be very high and can be measured by spectroscopy. The temperature rise can be derived

$$\Delta T_s = \frac{\sigma_s B_0^2}{8C_{sV} t_0} \left(1 - 1/\sqrt{\eta}\right)^2 \int_0^\tau \left\{ \begin{aligned} & (1-\tau)^2 + \frac{(2r_i - x_a)x_a}{r_0^2} + \frac{\mu_0 \sigma_t (1-\tau) [2r_i - d - x_a(t)] [d - x_a(t)]}{4t_0} \\ & + \frac{(2r_i - 2d - x_{sa})x_{sa}}{r_0^2} + \frac{\mu_0 \sigma_s (1-\tau) [2(r_i - d) - x_{sa}(t) - x'] [x' - x_{sa}(t)]}{4t_0} \end{aligned} \right\}^{-4+2/\sqrt{\eta}} \left\{ (1-\tau) [(r_i - d) - x'] \right\}^2 d\tau'$$

For an experimental design that the chamber inner radius and thickness takes 4 mm and 1 mm, respectively, it is easily found that once electrical conductivity of sample reaches 1×10^6 m/s or higher, the temperature rise could approach several thousand *Kelvin* and bring noticeable ablation at end of MFC, as is shown in Figure 13. As the MFC process continues, a large temperature rise begins from the outer surface of cylindrical sample to the center. And it may be detected by instantaneous multi-channel spectrum radiation method. Reversely, a detected large temperature rise may suggest IMT of sample under compression in chamber. A possible experimental design is shown in Figure 14.

5. Conclusion

In this work, magnetic flux compression (MFC) process was studied theoretically

by means of Maxwell equations. It is found that the MFC process can not be described by magnetic diffusion equations. Also revealed is that the whole MFC process, including eddy electric field distribution within liner, temperature rise of liner, the increase of magnetic field enclosed by a liner and so on may be dominated by a key dimensionless parameter, i.e., magnetic Reynolds number (MRN). To reach a magnetic field as high as possible, the MRN takes neither ultra-large nor quite small values. A notable Hall voltage exists at the liner, chamber and sample, and it can reach thousands of voltage at end of MFC, demonstrating that the normal resistance measurement method may not be suitable. Considering serious ablation of chamber and noticeable penetration of field into sample, a new method was proposed for probing insulator-metal transition of sample under isentropic compression, i.e., measuring temperature rise of sample in terms of instantaneous multi-channel spectroscopy. According to theoretical analysis, the related experimental designs were discussed. The theoretical analysis on MFC may assist people to understand the physical processes and improve related experimental designs.

References

- [1] G. V. Boriskov, S. I. Belov, A. I. Bykov, M. I. Dolotenko, N. I. Egorov, A. S. Korshunov, Yu. B. Kudasov, I. V. Makarov, V. D. Selemir, A. V. Filippov, Conductivity and Permittivity of Hydrogen Under Isentropic Magnetic Compression up to 3 Mbar, *J. Low Tem. Phys.* V.159, 307-310(2010).
- [2] Andreas A. Neuber, James C. Dickens, Magnetic Flux Compression Generators, *Proceedings of The IEEE*, Vol. 92, No. 7, (1205-1215)2004.
- [3] A. I. Pavlovskii, A. S. Kravchenko, V. D. Selemir, A. Y. Brodskii, Y. B. Bragin, V. V. Ivanov, I. V. Konovalov, V. G. Suvorov, K. V. Cherepenin, V. A. Vdovin, A. V. Korzhenevskii, and S. A. Sokolov, "EMG magnetic energy for superpower electromagnetic microwave pulse generation," in *Megagauss Magnetic Field Generation and Pulsed Power Applications*, M. Cowan and R. B. Spielman, Eds. Commack, NY: Nova, 1994, pp. 961–968.
- [4] A. I. Pavlovskii, R. Z. Lyudaeov, V. N. Plyashkevich, N. B. Romanenko, G. M. Spirov, and L. B. Sukhanov, "MCG application for powered channeling neodym laser," in *Megagauss Magnetic Field Generation and Pulsed Power Applications*, M. Cowan and R. B. Spielman, Eds. Commack, NY: Nova, 1994, pp. 969–976.
- [5] B. M. Novac and I. R. Smith, "Autonomous compact sources for high power microwave applications," presented at the Megagauss VII Conf., Tallahassee, FL, 1998.
- [6] Pavlovskii A.I., Kolokolchikov N.P., Tatsenko O.M., Bykov A.I., Dolotenko M.I., Karpikov A.A. Reproducible Generation of Multimegagauss Magnetic Fields. In:

Turchi P.J. (eds) Megagauss Physics and Technology. Springer, Boston, MA, (1980)
pp627-639

[7] A. I. Pavlovskii, A. I. Bykov, M. I. Dolotenko, et al., "Limiting value of reproducible magnetic field in cascade generator MC-1," in: *Megagauss Technology and Pulsed Power Applications: Proc. 4th Int. Conf. on Megagauss Magnetic Field Generation and Related Topics*, Santa Fe, 1986, New York-London (1987). pp. 37-54.

[8] C. M. Fowler, W. B. Garn, R. S. Caird, Production of Very High Magnetic field by Implosion, *J. Appl. Phys.* Vol. 31, No.3, 588-594(1960).

[9] D. Nakamura, Y. H. Matsuda, S. Takeyama, Precision of an Ultrahigh Magnetic Field Generated by Electro-magnetic Flux Compression, *J. Low Tem. Phys.* V.170, 457-462(2013).

[10] E. R. Parkinson, K. A. Jamison, J. B. Cornette, M. A. Cash, C. M. Fowler, and J. D. Goette, "Continued benchmarking of an FCG code," in *Proc. 12th IEEE Int. Pulsed Power Conf.*, 1999, pp. 724–727.

[11] A. Neuber, J. Dickens, J. B. Cornette, K. Jamison, R. Parkinson, M. Giesselmann, P. Worsey, J. Baird, M. Schmidt, and M. Kristiansen, "Electrical behavior of a simple helical flux compression generator for code benchmarking," *IEEE Trans. Plasma Sci.*, vol. 29, pp. 573–581, Aug. 2001.

[12] M.G. Giesselmann, T. Heeren, A. Neuber, and M. Kristiansen, "Advanced Modeling of an Exploding Flux Compression Generator Using Lumped Element Models of Magnetic Diffusion," *Proceedings of the IEEE Pulsed Power and Plasma Science Conference*, Las Vegas, NV (June 17-22, 2001), Eds. R. Reinovsky

and M. Newton, IEEE Catalog No. 0101CH37251, pp162-165.

[13] B.M. Novac, I.R. Smith, I.R., H.R. Stewardson, H.R., K. Gregory, and M.C.

Enache, "Two- Dimensional Modeling of Flux-Compression Generators", IEE

Symposium on Pulsed Power, IEE, London, pp 361-363 (April, 1998).

[14] Paton A., Millar W., Compression of Magnetic Field between Two Semi-Infinite

Slabs of Constant Conductivity, J. Appl. Phys. V. 35, N 4. (1964). P. 1121–1146.

[15] Lehner G. , Linhart J.G., and Somon J.P. Limitations on Magnetic Fields

Obtained by Flux-Compression: I // Nul. Fus. V. 4, (1964) P. 362–379.

[16] G.V. Boriskov, A.I. Bykov, N.I. Egorov, M.I. Dolotenko, V.N. Pavlov, V.I. Timareva,

Building zero isotherm of hydrogen isotopes taking into account experimental results of

isentropic compression up to pressures of several megabar, Journal of Physics: Conference

Series **121**, 072001(2008).

[17] 叶良修, 半导体物理学 (上册), 高等教育出版社, 第二版, 北京, (2007), PP147.

[18] A. I. Bykov, M. I. Dolotenko, N. P. Kolokolchikov, A. I. Pavlovskii, O. M.

Tatsenko, The cascade manetocumulative generator of ultrahigh magnetic field-A

reliable tool for megagauss physics, Physica B 216, 215-217 (1996).

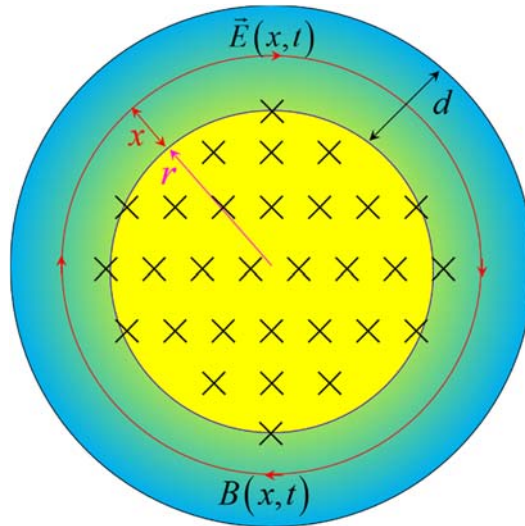


Figure 1. Schematic diagram for the liner configurations in the magnetic flux compression (MFC) process. The light blue region denotes the liner and yellow region denotes the liner cavity. Liner thickness is d and liner inner radius is r . The sign “ \times ” in yellow regions indicate that the magnetic field is perpendicular to the paper surface and point inwards. The vortex electrical current is shown by red circle lines. Position x begins from the liner inside.

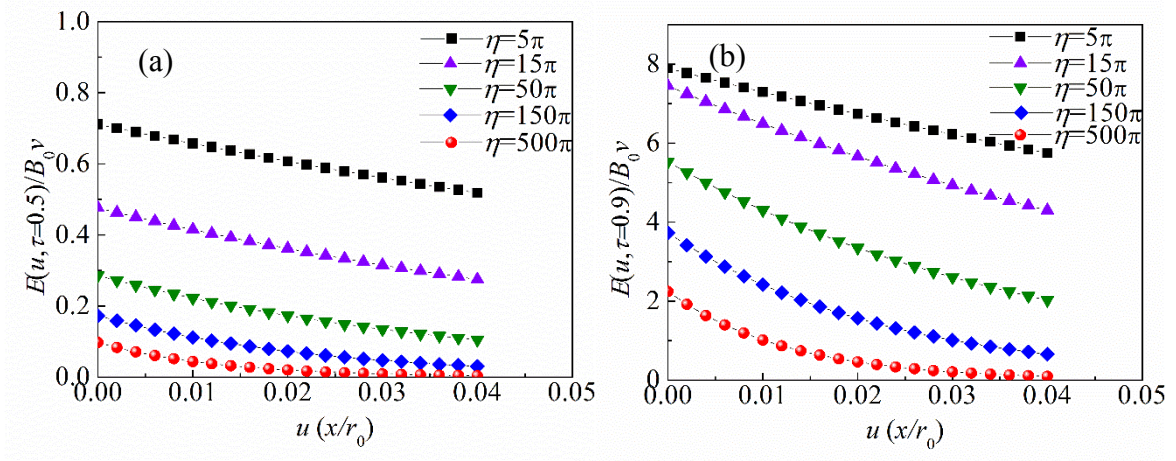


Figure 2. For liners with different magnetic Reynold number η , reduced eddy electric field $E(u, \tau)/B_0 v$ varies with reduced position $u=x/r_0$ at the liner. Reduced position u dependent of eddy electric field within liner at reduced time (a) $\tau=0.5$ and (b) $\tau=0.9$. The magnetic Reynold number is $\eta = \mu_0 \sigma v r_0 / 2$, where μ_0 is vacuum permittivity, σ is electrical conductivity of liner, B_0 is initial magnetic field, t_0 is the duration time $t_0=r_0/v$, v is flying velocity of liner inside, and r_0 is initial inner radius of liner.

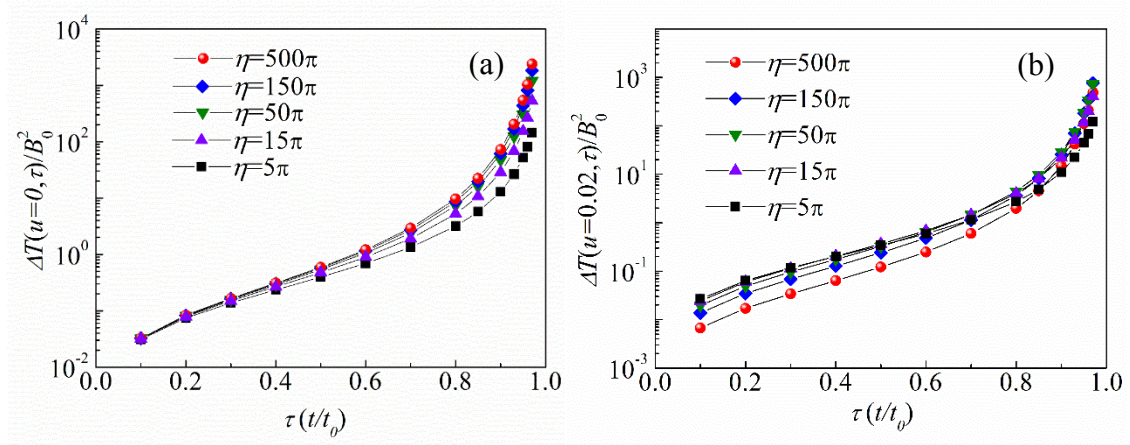


Figure 3. Reduced time dependent of temperature rise for liners with different magnetic Reynolds numbers. The specific heat capacity is taken to be $3 \times 10^6 J/(K \cdot m^3)$ as an estimation. (a) Temperature rise versus reduced time for liner inside; (b) temperature rise versus reduced time for reduced position $u=0.02$ at liner.

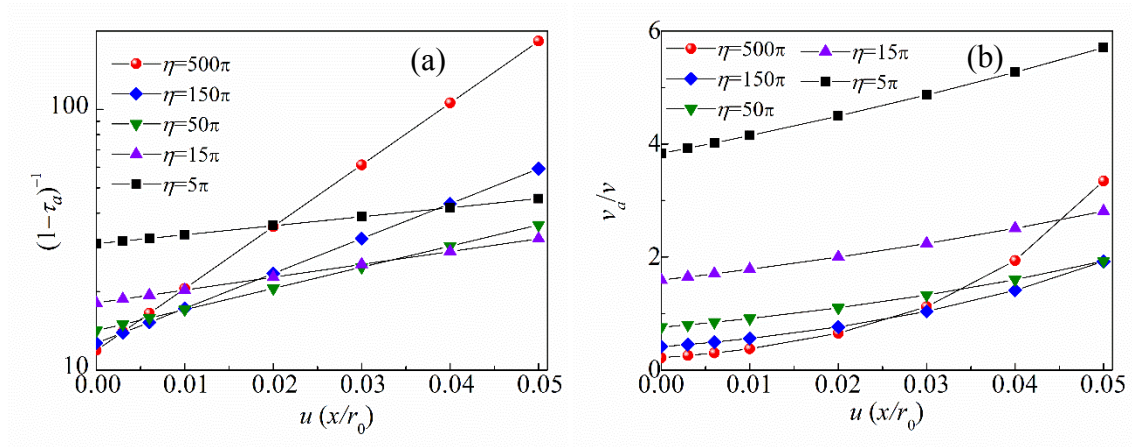


Figure 4. (a) Reduced initial ablation time (τ_a) and (b) reduced ablation velocity versus reduced position ($u=x/r_0$) for liners with different magnetic Reynolds numbers η . In the calculation, the specific heat capacity the initial magnetic field is taken to be $3 \times 10^6 \text{ J}/(\text{K} \cdot \text{m}^3)$ and 5 T , respectively, and the ablation temperature is assumed to be 3000 K at which the electrical conductivity could be regarded as zero.

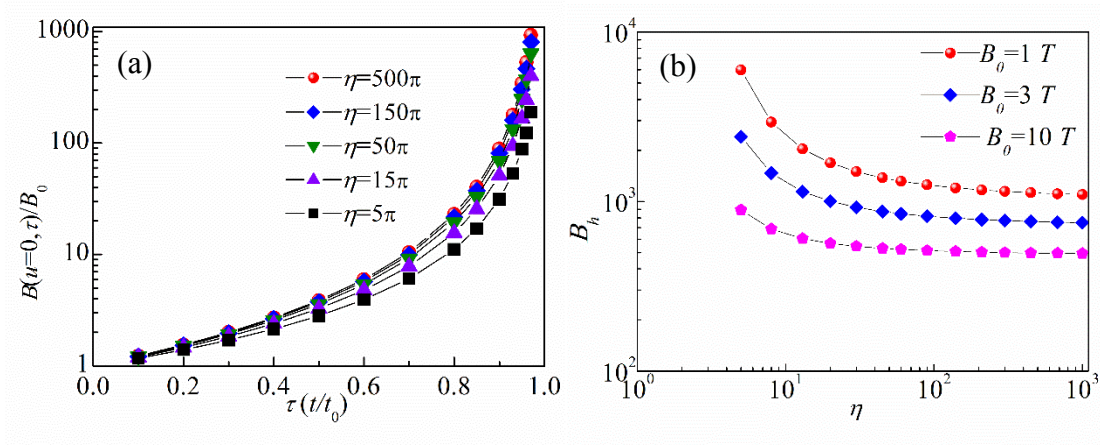


Figure 5. (a) Reduced magnetic field varies with reduced time for liners with different magnetic Reynold numbers (MRN) η . t_0 is total duration time of MFC process. Black quadrangle for magnetic Reynold number 5π ; violet triangle for magnetic Reynold number 15π ; green triangle for magnetic Reynold number 50π ; blue quadrangle for magnetic Reynold number 150π ; red circled for magnetic Reynold number 500π ; (b) For liners with different initial magnetic field B_0 , MRN η dependent of highest magnetic field obtained within liner. Red circled, blue quadrangle and magenta pentagon stands for MRN- B_h relations under initial field $1 T$, $3 T$, $5 T$, respectively.

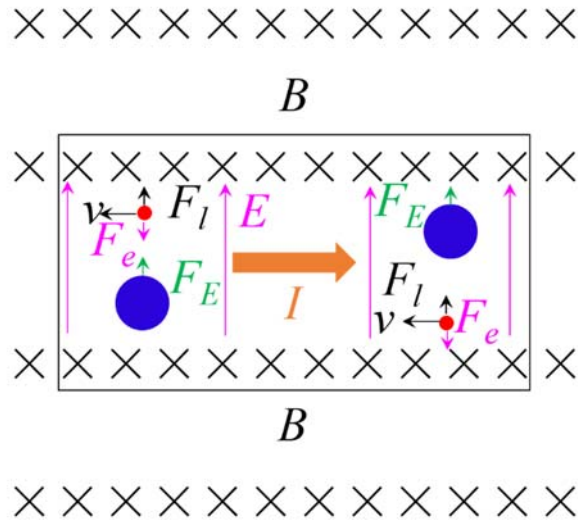


Figure 6. Sketch of forces on electron and ions in a part of liner under magnetic field B . I is the electrical current flowing through this part of liner and v is average drifting velocity of free electrons, the induced Hall electric field is E . The free electrons experience Lorentz force F_l and attractive force F_e from ions. The ions are also subject to counterforce F_E .

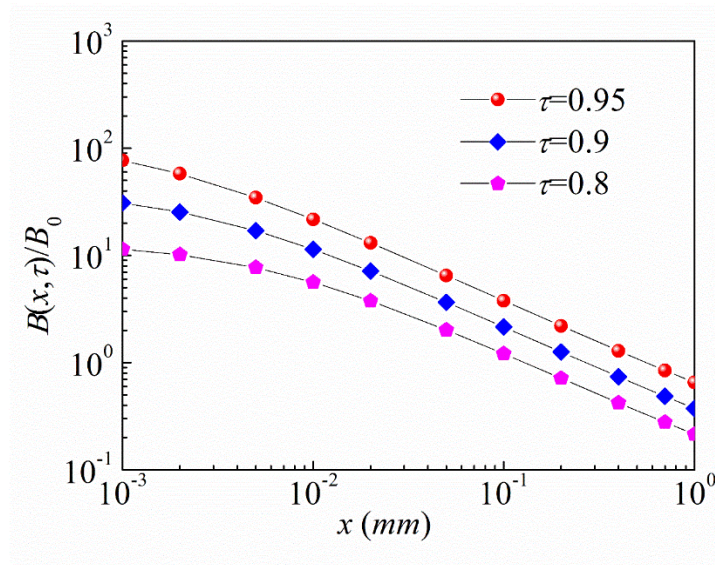


Figure 7. Distribution of magnetic field at the metallic sample chamber at different reduced time. Red circle, blue square, magenta pentagon denote magnetic field versus distance from chamber outside at reduced time 0.95, 0.9, 0.8, respectively. In the calculation, total duration of MFC takes a typical value, $t_0=10 \mu s$, and the MRN value takes $\eta=25$. The chamber is selected to be a pure copper (electrical conductivity takes a value $60 \times 10^6 \text{ s/m}$) with thickness 1 mm and outside radius $r_i=5 \text{ mm}$.

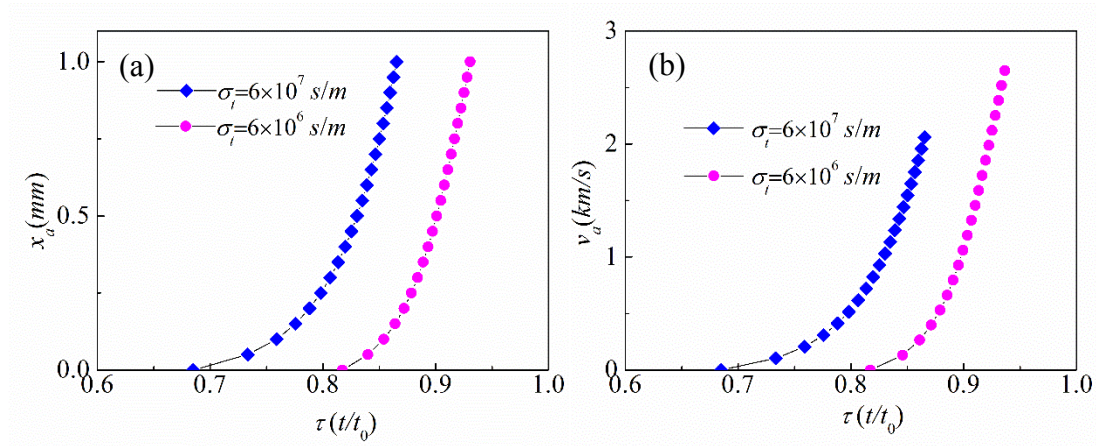


Figure 8. Ablation thickness (a) and ablation velocity (b) of copper chamber versus reduced time. In the calculations, the magnetic field outside the chamber takes the form $B(0, \tau) \approx B_0(1 - \tau)^{-1.6}$, the initial magnetic field B_0 takes 5 T. The outer radius of chamber takes 5 mm. When the temperature rise reaches 3000 K, the ablation is regarded to occur. (a) Magenta circled (the electrical conductivity takes the approximate value at room temperature 6×10^7 s/m) and blue squared curves (the electrical conductivity takes the approximate value upon melting 6×10^6 s/m) give variations of ablation thickness and can be fitted well by $x_a \approx \exp(20.6\tau - 17.8)$, and $x_a \approx \exp(26.3\tau - 24.4)$, respectively; (b) Magenta circled and blue squared curves give ablation velocity along chamber radius.

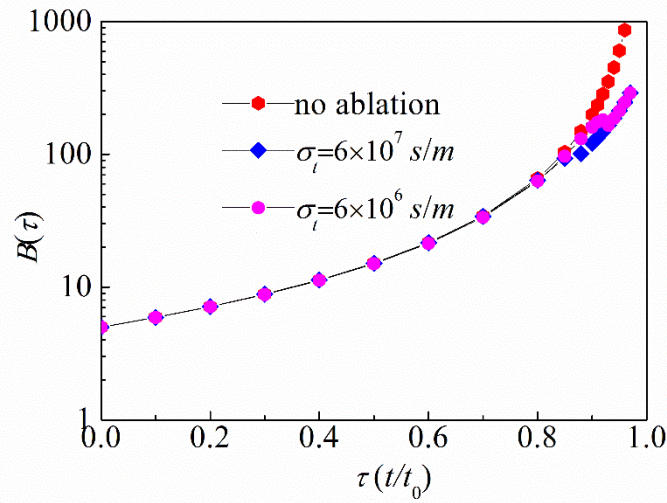


Figure 9. Reduced time dependent of magnetic field outside the chamber. Red pentagons give the field in the case of chamber without ablation; blue squared denotes the case of chamber with electrical conductivity 6×10^7 s/m; magenta circled gives the case of chamber with electrical conductivity 6×10^6 s/m. In the calculation based on equation (20), root square of MRN takes 5 and the initial magnetic field B_0 takes 5 T. The outer radius of chamber takes 5 mm.

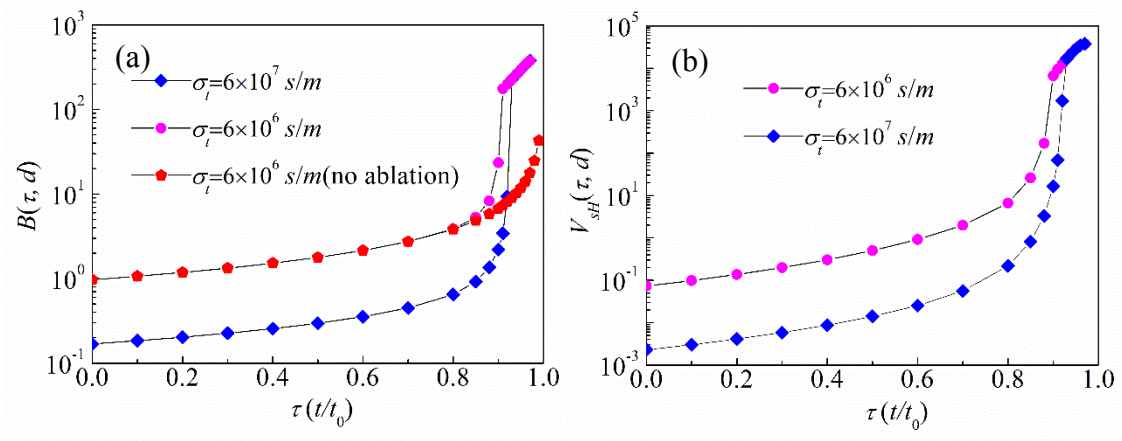


Figure 10. Reduced time dependent of magnetic field (a) and Hall electrical voltage (b) on the non-conducting sample. The carrier mobility is assumed to be $0.1 \text{ m}^2/Vs$ in the sample, the magnetic field takes form of Equation (22) where initial magnetic field B_0 takes 5 T , outer radius of the chamber and its thickness takes 5 mm and 1 mm as before. Magenta circled and blue squared denote results for the chamber with invariant electrical conductivity $6 \times 10^6 \text{ s/m}$ and $6 \times 10^7 \text{ s/m}$, respectively.

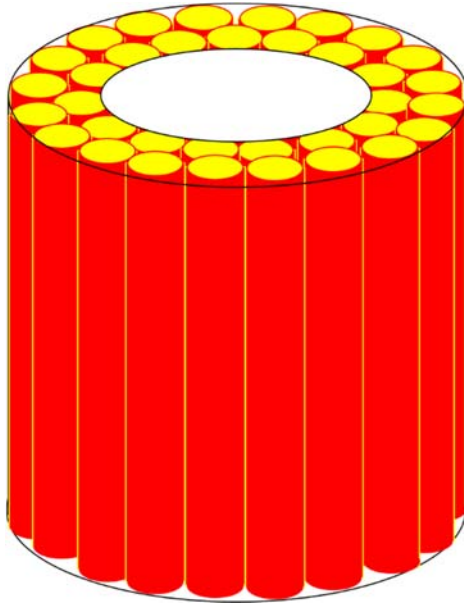


Figure 11. Sketch of supreme cascade for magnetic flux compression (MFC). This cascade consists of many straight metal wires with insulating film on their surface outside. At normal state this cascade is insulating along its circumference, however, it becomes conducting upon penetration of shock waves. The shock waves may compress the wires, causing destruction of insulating films and welding of these metal wires, so that the cascade becomes a liner which is electrically conductive and permit large eddy electrical currents.

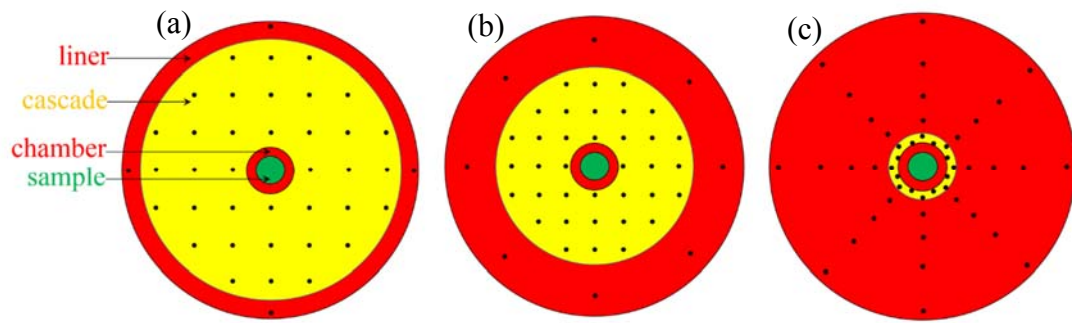


Figure 12. Schematic diagrams for the supreme cascade transforming into a liner and compressing magnetic flux. The yellow region denotes the initial cascade consist of insulating-film-coated straight metal wires. The outer red regions give the liner constructed by the welded metal wires under shock waves and it becomes thicker and thicker as propagation of shock waves. The inner red ring stands for the sample chamber and the green region is the sample. Black dots denotes the magnetic lines and more concentrated dots indicate a stronger magnetic field. The signs “ • ” indicate that the magnetic field is perpendicular to the paper surface and point outwards. (a) at the beginning of magnetic flux compression (MFC); (b) in the middle of MFC; (c) at the end of MFC.

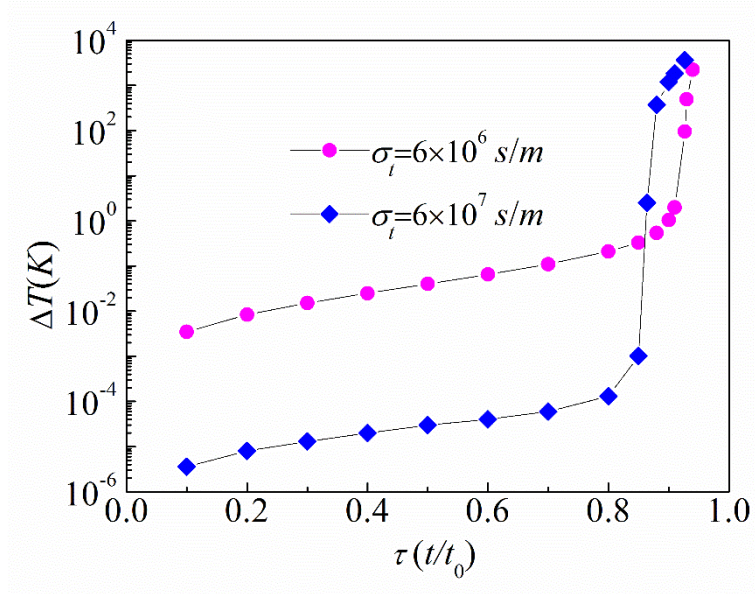


Figure 13. Reduced time dependence of temperature rise for sample with electrical conductivity $1 \times 10^6 \text{ s/m}$ at the contact interface with chamber. In the calculation, the radius and thickness of chamber take 5 mm and 1 mm , respectively. The magenta circles and blue squares denotes chamber with electrical conductivity $6 \times 10^6 \text{ s/m}$ and $6 \times 10^7 \text{ s/m}$, respectively.

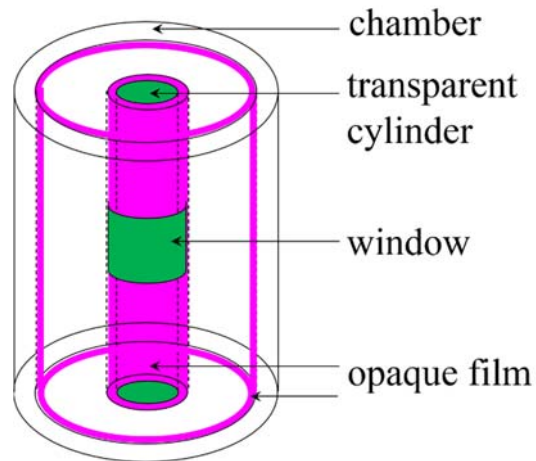


Figure 14. Sketch of a new method for resistance measurement. At center of chamber, a transparent cylinder (green zones) is inserted in. At the cylindrical surface of chamber inside and transparent cylinder outside, a non-conducting opaque film (magenta regions) is deposited. In the middle of this film on transparent cylinder, a window is retained for temperature measurement by means of instantaneous multi-channel spectrum radiation method. And the spectrum could be collected from two ends of transparent cylinder.